Materials and methods

Cell culture and immunostaining

Human Primary Pulmonary Artery Endothelial Cells (HPAEC, ATCC PCS-100-022) were cultured in the Endothelial Cell Medium (ScienCell Cat. #1001) supplemented with 10% fetal bovine serum (FBS, Gibco 16140071). For immunostaining, about 2×10^5 cells were plated on poly-D-Lysine (Gibco A3890401) coated cell imaging dish (MatTek P35G-1.5-14-C) and maintained at 37 ℃ with 5% CO_2 overnight. After rinsing once with Phosphate Buffer Saline (PBS), cells were fixed by -20 ℃ pre-chilled 100% methanol at room temperature (RT) for 8 min, followed by three PBS washes. Cells were then blocked with PBST (PBS + 0.1% Tween 20) supplemented with 1% BSA and 22.52 mg/mL glycine for 1h. Blocking buffer was removed and cells were incubated with primary antibody solution (1:500 dilution of anti-NDUFS1 rabbit polyclonal antibody and anti-COX4I1 mouse monoclonal antibody in PBST with 1% BSA) overnight with gentle shaking and light avoidance. Then, cells were washed with PBS for three times followed by secondary antibody incubation (Genvivo Biotech, Gen FlourTM Red anti-rabbit, and Gen FlourTM Green anti-mouse, 1:500 dilution in PBST with 1% BSA) for 1h away from light, and then PBS washing step was repeated for three times.

In vivo STED image acquisition

Stimulated emission depletion (STED) microscopy was performed on Leica TCS SP8 gSTED 3X microscope equipped with hybrid detectors (HyD), white light laser (WLL), 592nm, 660nm and 775nm STED depletion lasers, as well as the Application Suite X software (LAS X; Leica Microsystems). Images were acquired using the high-contrast plan apochromat 100×, 1.40 NA oil CS2 objective lens. NDUFS1 fluorescence was excited by WLL at 561nm with 15% intensity under 85% output power, and the emission depletion was accomplished with 660nm STED laser (50% intensity under 60% output power). Its fluorescence was detected at 575-646nm, with 0.8-10.0 ns time gating using the HyD detector. COX4I1 fluorescence was excited by WLL at 488nm with 8% intensity under 85% output power, and the 592nm STED laser (90% intensity under 20% output power) was used for emission depletion. The COX4I1 fluorescence between 500-580nm was collected with 1.0-6.0 ns time gating. STED images were captured at 1,024×1,024 pixel with pixel size of 19nm.

Mitochondria isolation

Mitochondria from porcine heart was kept on ice for all procedures and prepared as described previously [52]. The hearts of eight- to ten-month-old healthy male pigs (Sus scrofa) were bought from the on-campus slaughterhouse in Tsinghua University. All animal maintenance and experimental procedures used in the current study were carried out according to the guidelines of the Institutional Animal Care and Use Committee (IACUC) of Tsinghua University, Beijing, China. Briefly, heart muscles were cut into small cubes, washed twice with Milli-Q water and suspended in 1 mL Buffer A (50 mM HEPES pH 7.5, 225 mM sorbitol, 75 mM sucrose, 20 mM KCl, 1mM EGTA and 0.1% BSA). These tissues were homogenized in a large-capacity blender for 5 min. The homogenate was centrifuged at 3,000 ×*g* for 20 min. The supernatant was further centrifuged at 20,000×*g* for 30 min to obtain the crude mitochondrial pellet. Crude mitochondria were suspended in 200 mL Buffer B (20 mM HEPES pH 7.5, 250 mM sucrose, 20 mM KCl and 40% Percoll) and centrifuged at 60,000 ×*g* for 50 min. The clear mitochondria layer was aspirated carefully and diluted with 50mL Buffer C (10 mM HEPES pH 7.5, 75 mM sorbitol, 75 mM sucrose and 20 mM KCl). The pure mitochondria were obtained after centrifugation at 20,000 ×*g* for 30 min.

Megacomplex purification

Pure porcine heart mitochondria were solubilized using 1% (w/v) digitonin for 1h with slow stirring in Buffer C at 4 ℃. The extraction was centrifuged at 150,000 ×*g* for 30 min at 4 ℃, and the supernatant was concentrated to 1 mL by 100 kDa cutoff centrifugal filter (Millipore). Then, the concentrated sample was loaded and centrifuged on 0.3-1.3 M sucrose gradients in Buffer D (10 mM HEPES, pH 7.5, 20 mM KCl and 0.1% digitonin) at 150,000 ×*g* for 20 h at 4 ℃ with an SW41 Ti rotor (Beckman). Gradients were fractionated and investigated by 3-10% acrylamide gradient gel for BN-PAGE (Blue native PAGE) [53] and NBT (Nitro blue tetrazolium) staining [54]. The purified megacomplexes were concentrated and finally purified by Superose 6 Increase 10/300 GL column (GE Healthcare) in Buffer D. The fractions containing a relatively high proportion of megacomplex were collected for Cryo-EM sample preparation.

Cryo-EM sample preparation and data acquisition

Aliquots (4 μL) of megacomplex complex (0.3 mg/mL) were applied to freshly continuous thin layer of carbon grids (Quantifoil 300-mesh Au R1.2/1.3, Micro Tools GmbH, Germany) and glow discharged for 30 s. The grids were blotted for 1.5 s and plunged into liquid ethane in 100% humidity at 8 ℃ with Mark IV Vitrobot (Thermo Fisher Scientific). Raw movie stacks were collected using a Titan Krios microscope (Thermo Fisher Scientific) operated at 300 kV by a K3 Summit direct electron detector and a GIF Quantum energy filter (Gatan). All data were collected using SerialEM software at a nominal magnification of 81,000 × in super-resolution mode with a slit width of 20 eV and the defocus range were set from -1.3 μm to -2.3 μm. Five batches of data were collected with six cryo-samples with same protein preparation, obtaining 41,117 micrographs with a total dose of 50 e/$Å^2$ and exposure time of 3 s.

Image processing

In general, movies were motion-corrected using MotionCor2 [55]. Gctf was used to determine the contrast transfer function (CTF) parameter and produce the CTF power spectrum on basis of summed micrographs [56]. Particles were auto-picked on dose-weighted micrographs using Gautomatch (www.mrclmb.cam.ac.uk/kzhang/Gautomatch/). Briefly, about 1,000 particles were selected and generated 2D averages templates for particle auto-picking and 2,733,141 particles were extacted from manually selected micrographs. Micrographs showed that the megacomplex accounted for ~10% of the particles and the remaining particles were various forms of the $SCI_1III_2IV_1$. The previously reported 17.4 Å model of human $MCI_2III_2IV_2$ (PDB: 5XTI) was low-pass filtered to 40 Å for initial model [23]. All extracted particles using a box size of 480 and a binned pixel size of 6.6 Å, were subjected to two rounds of 2D classification and three rounds of 3D classification using C1 symmetry and 297,608 particles were retained. 239,014 selected particles from eight classes indicating expanded $MCI_2III_2IV_2$ which CIV had separated to $CIII_2$ and directly formed interaction with CI membrane arm, were carried out finally 3D classification of $MCI_2III_2IV_2$. The other two classes were selected to indicate constricted $MCI_2III_2IV_2$ which CIV was apart from CI membrane arm and interacted directly with $CIII_2$. Two

different states containing 96,592 and 47,714 good particles were subjected to 3D auto-refinement without symmetry in RELION 3.1[57], which defined as constricted and expanded $MCI_2III_2IV_2$.

As the flexibility of the megacomplex indicated several existing conformations of CI within $CIII_2$ and CIV, we classified these states by signal subtracting around the CI, followed by focused 3D classification without image alignment. Briefly, expanded CI^A was signal subtracted based on the refined map of expanded $MCI_2III_2IV_2$ with soft mask, then particles were subjected to 3D auto-refine and 3D classification without image alignment, which resulted in two states of CI^A. Based on the coordinates of expanded active CI^A and expanded deactive CI^A, the opposite expanded CI^B particles were re-extracted and performed the same procedure to expanded CI^A, which also resulted in two states of CI^B. Finally, three kinds of particles of expanded active CI^A & active CI^B with 10,060 particles, expanded active $CI^{A(B)}$ & deactive $CI^{B(A)}$ with 22,767 particles and expanded deactive CI^A & deactive CI^B with 35,332 particles were obtained, we reverted the signal for CI and obtain 3D reconstructions of these three states of expanded $MCI_2III_2IV_2$, which were separately subjected to non-uniform refinement and local refinement in cryoSPARC software [58]. The $MCI_2III_2IV_2$ particles containing expanded active CI^A & active CI^B was named State 1, which produced an overall resolution of 5.09 Å with C1 symmetry and 5.09 Å with imposed C2 symmetry. The $MCI_2III_2IV_2$ particles containing expanded deactive CI^A & deactive CI^B was named Mid 1, which performed an overall resolution of 3.84 Å with C1 symmetry and 3.46 Å with imposed C2 symmetry. The $MCI_2III_2IV_2$ particles consisting of expanded active $CI^{A(B)}$ & deactive $CI^{B(A)}$ was named Mid 2, which performed an overall resolution of 4.32 Å with C1 symmetry. Selected particles of three states were signal subtracted of $CIII_2$ and CIV, and then subjected to local re-alignment and 3D classification without alignment with a soft mask. Meanwhile, Signal subtraction for constricted-$CI^{A/B}$ particles based on the refined map of constricted $MCI_2III_2IV_2$ with soft mask were subjected to 3D auto-refine and 3D classification without image alignment, which resulted in only deactive $CI^{A/B}$ interestingly. The particles of constricted $MCI_2III_2IV_2$ were classified into two states using ab initio reconstruction and heterogeneous refinement. One state of two CIVs had separated to CI membrane arm and formed directly interaction with $CIII_2$ which was named State 2, another state of CIV had separated to $CIII_2$ and opposite CIV formed directly interaction with $CIII_2$ which was named Mid 3. The particles of these two states were

separately subjected to non-uniform refinement and local refinement in cryoSPARC software [58], State 2 of $MCI_2III_2IV_2$ was performed an overall resolution of 4.05 Å with C1 symmetry and 3.58 Å with imposed C2 symmetry, Mid 3 of $MCI_2III_2IV_2$ was performed an overall resolution of 4.32 Å with C1 symmetry. In order to obtain a high-resolution reconstruction of $CIII_2$ and CIV, all good particles of active CI, deactive CI, $CIII_2$ and CIV were separately merged, refined three rounds of CTF parameter refinement and postprocessed separately to give final maps at 3.34 Å, 3.22 Å, 3.36 Å and 3.66 Å, respectively. We performed 3D variability analysis (3DVA) in cluster mode with a mask around Rieske head domain in State 1, Mid 1 and State 2 in cryoSPARC software [45]. The cluster analysis with the Rieske head domain was subjected to three series and led to one state nearly: Rieske head domain of State 1 in the "*b*" state, Mid 1 in the "*Int*" state and State 2 in the "c_1" state. In each round of 3DVA displayed interpretable molecular motions. All reported resolutions are based on the gold-standard FSC=0.143 criteria, and the final FSC curves were corrected for the effect of a soft mask by using high-resolution noise substitution. The final density maps were sharpened by B-factors calculated with the RELION post-processing program. The final maps for model building and figure presentation were performed using DeepEMhancer [59]. All composite maps of these five $MCI_2III_2IV_2$ were generated in UCSF Chimera using 'vop maximum' command and used for model building and refinement [60]. Further information for all samples is provided in Supplementary Table 1. Local resolution map was calculated using ResMap [61].

Atomic model building and refinement

The composite density maps of $MCI_2III_2IV_2$ in different states and the sub-region complexes were used for the model building. Generally, for atomic models of porcine active- and deactive- CI, 3.7 Å human CI structure (PDB: 5XTD) as homology model was fitted into the 3.34 Å active- and 3.22 Å deactive- CI densities in UCSF Chimera [23]. Two CI models were manually adjusted and refined using COOT [62]. Finally, all the 14 core subunits and 31 supernumerary subunits were assigned into the CI maps. Based on the 3.36 Å density map of $CIII_2$, 3.4 Å human $CIII_2$ structure (PDB: 5XTE) was chosen as the initial model, the atomic models of porcine $CIII_2$ with 23 subunits (two UQCRFS1N and two *Cyt.c* subunits) was built and refined by the same procedure as mentioned before [23]. We were able to

model side chains and local geometry to higher accuracy. To build atomic models of porcine CIV, we used 3.6 Å human structure (PDB: 5Z62) as the initial model [41]. Based on the 3.91 Å density map, the final CIV model with 14 subunits was built and refined by the same procedure as mentioned before. We docked all atomic models of sub-region complexes in five $MCI_2III_2IV_2$ maps in UCSF Chimera and merged all the coordinates into final PDB files in COOT, respectively. All ligands and phospholipids models were generated using elbow module in PHENIX by their geometric constraints [63]. The ligands and phospholipids were docked into densities and refined in COOT. All the figures were created in PyMOL (www.pymol.org), COOT and UCSF Chimera [60] and Chimera X [64]. For cross-validation against overfitting, we randomly displaced the atom positions of the final model by up to a maximum of 0.5 Å, and refined against the composite maps of $MCI_2III_2IV_2$ using real-space refinement module in PHENIX, respectively [65]. The stereochemical quality of each model was assessed using MolProbity [66]. Finally, our results establish that each structure $MCI_2III_2IV_2$ contains 140 subunits (69 different kinds) in total with 240 transmembrane helices (TMHs, CI: 78, $CIII_2$: 26 and CIV: 29, respectively) and has a molecular weight of about 2.9 MDa. Statistics for model refinement and validation are shown in Supplementary Tables 1-3.

References

52 Gu, J. *et al.* The architecture of the mammalian respirasome. *Nature* **537**, 639-643, doi:10.1038/nature19359 (2016).

53 Wittig, I., Braun, H. P. & Schagger, H. Blue native PAGE. *Nat Protoc* **1**, 418-428, doi:10.1038/nprot.2006.62 (2006).

54 Kuonen, D. R., Roberts, P. J. & Cottingham, I. R. Purification and analysis of mitochondrial membrane proteins on nondenaturing gradient polyacrylamide gels. *Analytical Biochemistry* **153**, 221-226, doi:10.1016/0003-2697(86)90084-9 (1986).

55 Zheng, S. Q. *et al.* MotionCor2: anisotropic correction of beam-induced motion for improved cryo-electron microscopy. *Nat Methods* **14**, 331-332, doi:10.1038/nmeth.4193 (2017).

56 Zhang, K. Gctf: Real-time CTF determination and correction. *J Struct Biol* **193**, 1-12, doi:10.1016/j.jsb.2015.11.003 (2016).

57 Zivanov, J. *et al.* New tools for automated high-resolution cryo-EM structure determination in RELION-3. *Elife* **7**, doi:10.7554/eLife.42166 (2018).

58 Punjani, A., Rubinstein, J. L., Fleet, D. J. & Brubaker, M. A. cryoSPARC: algorithms for rapid unsupervised cryo-EM structure determination. *Nat Methods* **14**, 290-296, doi:10.1038/nmeth.4169 (2017).

59 Sanchez-Garcia, R. *et al.* DeepEMhancer: a deep learning solution for cryo-EM volume post-processing. *Commun Biol* **4**, 874, doi:10.1038/s42003-021-02399-1 (2021).
60 Pettersen, E. F. *et al.* UCSF Chimera--a visualization system for exploratory research and analysis. *J Comput Chem* **25**, 1605-1612, doi:10.1002/jcc.20084 (2004).
61 Swint-Kruse, L. & Brown, C. S. Resmap: automated representation of macromolecular interfaces as two-dimensional networks. *Bioinformatics* **21**, 3327-3328, doi:10.1093/bioinformatics/bti511 (2005).
62 Emsley, P. & Cowtan, K. Coot: model-building tools for molecular graphics. *Acta Crystallogr D Biol Crystallogr* **60**, 2126-2132, doi:10.1107/S0907444904019158 (2004).
63 Moriarty, N. W., Grosse-Kunstleve, R. W. & Adams, P. D. electronic Ligand Builder and Optimization Workbench (eLBOW): a tool for ligand coordinate and restraint generation. *Acta Crystallogr D Biol Crystallogr* **65**, 1074-1080, doi:10.1107/S0907444909029436 (2009).
64 Pettersen, E. F. *et al.* UCSF ChimeraX: Structure visualization for researchers, educators, and developers. *Protein Science* **30**, 70-82, doi:10.1002/pro.3943 (2021).
65 Afonine, P. V. *et al.* Real-space refinement in PHENIX for cryo-EM and crystallography. *Acta Crystallogr D Struct Biol* **74**, 531-544, doi:10.1107/S2059798318006551 (2018).
66 Williams, C. J. *et al.* MolProbity: More and better reference data for improved all-atom structure validation. *Protein Sci* **27**, 293-315, doi:10.1002/pro.3330 (2018).

Extended data figures and figure legends

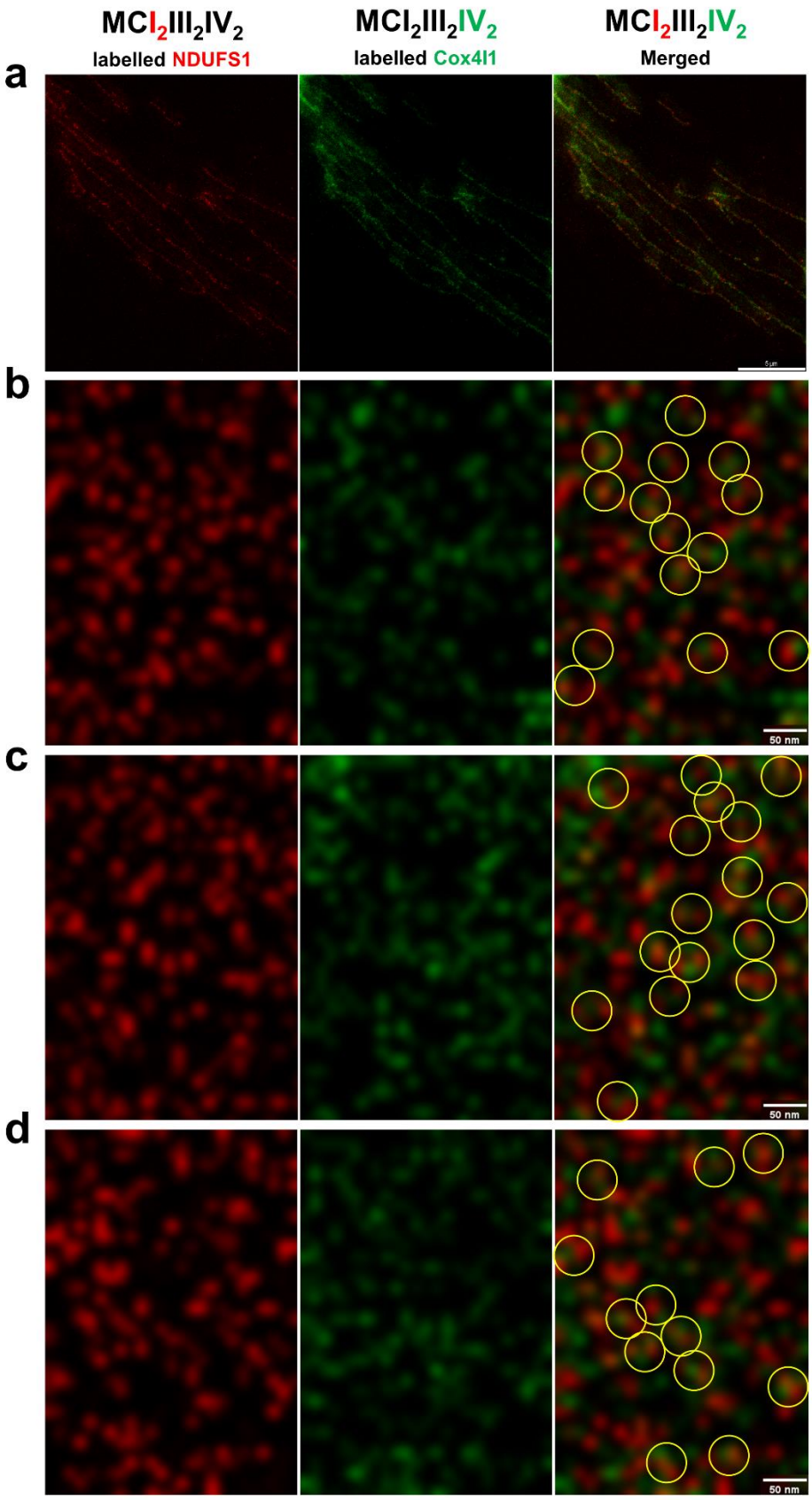

Extended Data Fig. 1 | Super-resolution optical microscopy of fixed cell samples.

a-d, The immunofluorescence STED images of NDUFS1(left) and COX4I1(middle) in HPAEC, the merged image is shown on the right. These two-fluorescence representing two subunits of megacomplex display similar distribution, which indicates the same mitochondria. Representative images of fluorescent immunostaining of $MCI_2III_2IV_2$ with anti-NDUFS1 (red) and anti-COX4I1 (green), respectively. Four-points fluorescence pattern of $MCI_2III_2IV_2$ was selected from the magnified merged image. Scale car, 5μm.

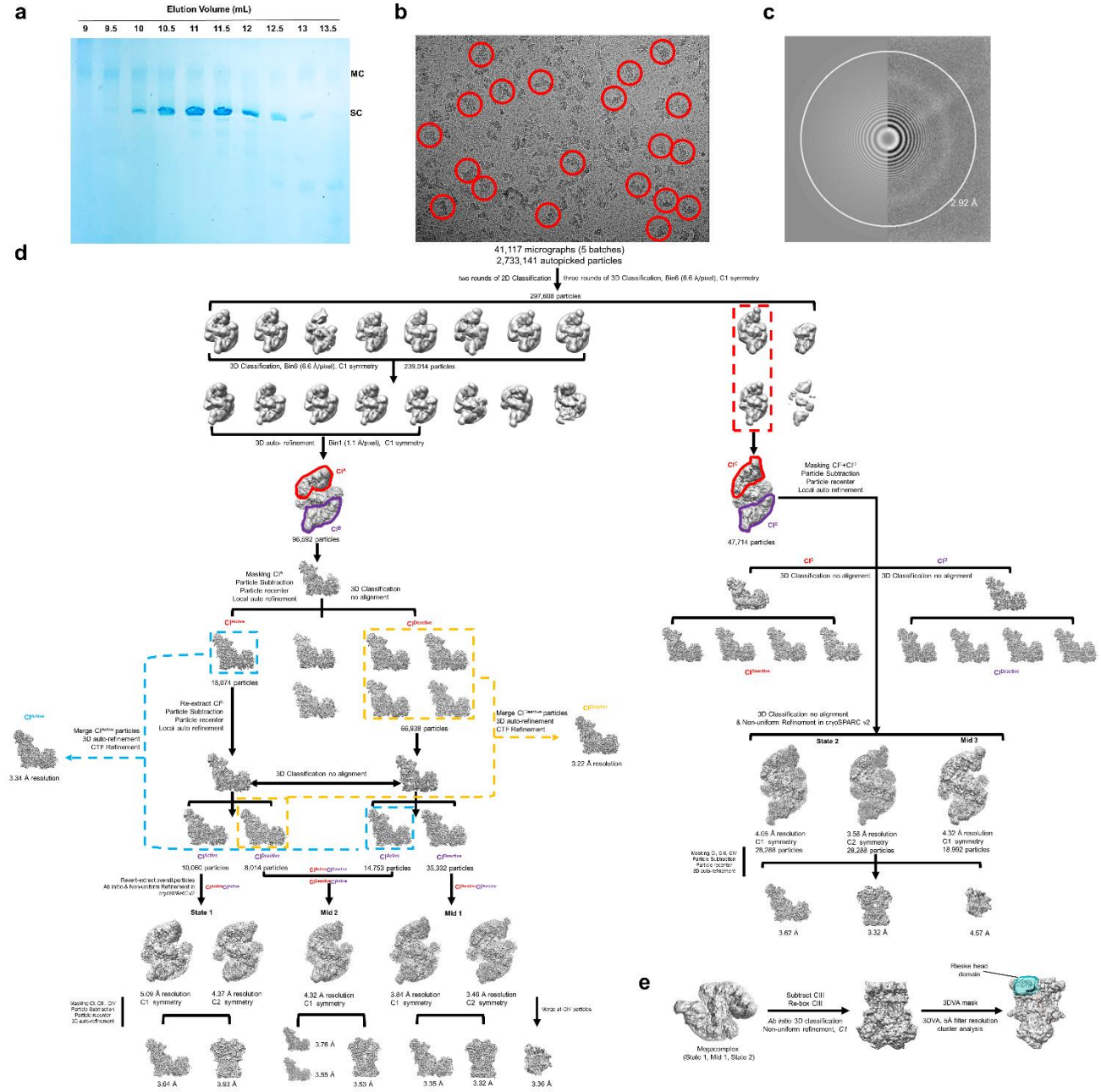

Extended Data Fig. 2 | Biochemical characterization and cryo-EM workflow scheme for porcine $MCI_2III_2IV_2$ structures.

a, Fractions of size-exclusion chromatography were analyzed by BN-PAGE.

b, A representative Cryo-EM micrograph of the $MCI_2III_2IV_2$. The $MCI_2III_2IV_2$ particles are labeled by red circles.

c, Power-spectrum of the micrograph in panel **b**.

d, For data processing of the porcine $MCI_2III_2IV_2$, five batches of data were collected and 41,117 micrographs and 2,733,141 particles were obtained in total. 239,014 particles were subjected to several rounds of 3D classification for $MCI_2III_2IV_2$. Signal subtraction, 3D-auto refinement, CTF Refinement and post-processing were performed with different sub-regions in RELION 3.1[57].

e, 3D variability analysis workflow of Rieske head domain region in $CIII_2$. Detailed procedures were described in Methods[45].

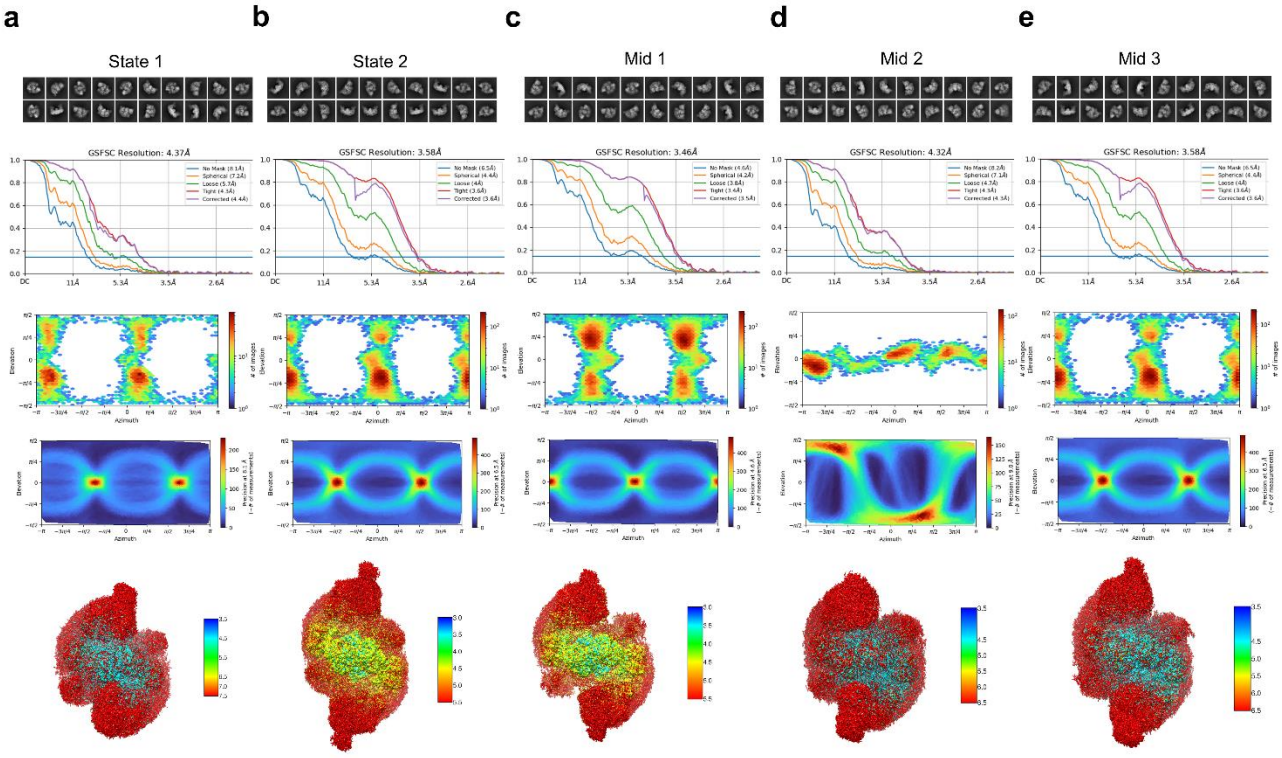

Extended Data Fig. 3 | Statistics of the final density maps of porcine $MCI_2III_2IV_2$.

a-e, Representative 2D class averages (upper), gold-standard Fourier Shell Correlation (FSC=0.143) curves (lower), particle orientation distributions (middle) and local resolution maps (bottom) viewed

from the matrix region of $MCI_2III_2IV_2$ of State 1, State 2 and Mid 1-3. The color scale is shown in right.

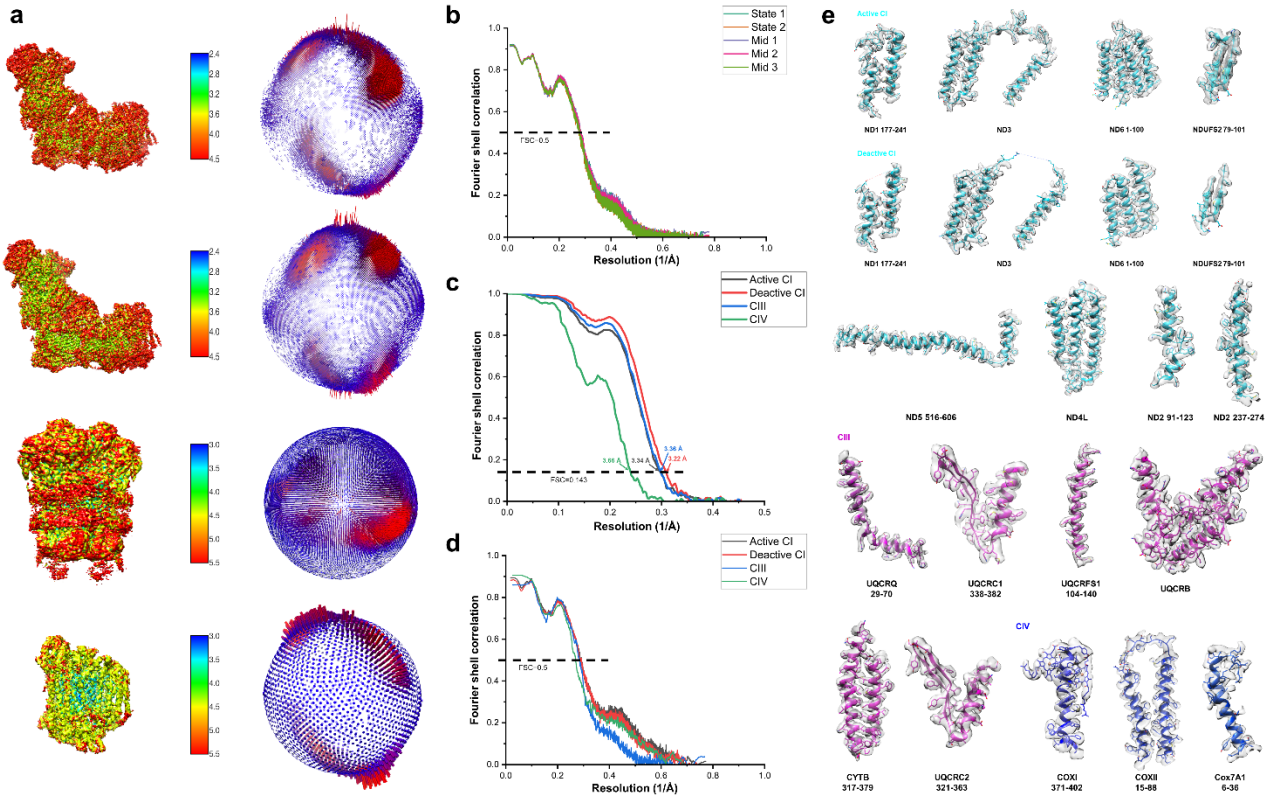

Extended Data Fig. 4 | Statistics of the final density maps of CI, CIII and CIV.

a, Local resolution map of the final 3D density map, particle orientation distributions of active CI, deactive CI, $CIII_2$ and CIV. The color scale is shown in middle.

b, Cross-validation with the maps and models curves (FSC=0.5) of $MCI_2III_2IV_2$ of State 1, State 2 and Mid 1-3.

c, Gold-standard Fourier Shell Correlation (FSC=0.143) curve of the final density maps. The final resolution of active- and deactive CI, $CIII_2$, CIV are 3.34, 3.22, 3.36, 3.66 Å, respectively.

d, Cross-validation with the maps and models curves (FSC=0.5) of active CI, deactive CI, $CIII_2$ and CIV.

e, Electron density maps of each segment of CI, $CIII_2$ and CIV. Structural differences between active CI (upper panel) and deactive CI (lower panel) of ND1, ND3, ND6 and NDUFS2 subunits. The boundaries of each displayed segment are labelled. The densities, shown as grey meshes, are contoured at 3–4σ in Chimera. The disordered loops of $Glu202–Ala216_{ND1}$, $Thr34–Ala47_{ND3}$ and $Gln87–His92_{S2}$ regions are indicated by dashed lines, and poorly resolved $Glu77–Leu122_{ND6}$ region is not shown in

deactive CI. Electron density maps of each segment of CI, $CIII_2$ and CIV. The boundaries of each displayed segment are labelled. The densities, shown as grey meshes, are contoured at 3–4σ in Chimera. CI, $CIII_2$ and CIV are colored and labeled with texts in same colors, respectively.

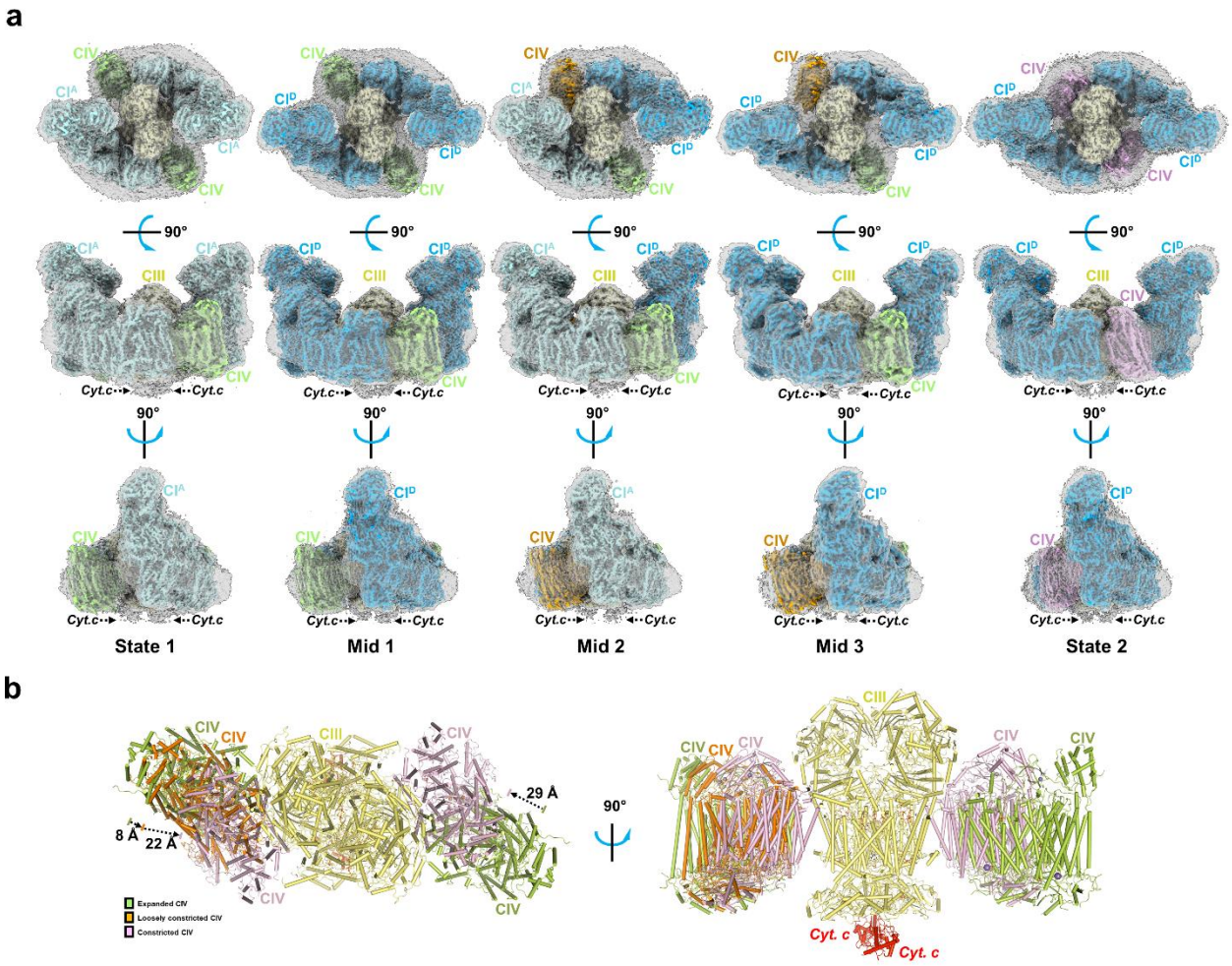

Extended Data Fig. 5 | The density maps and conformational changes of $MCI_2III_2IV_2$ structures. **a,** The high-resolution maps of five-states of $MCI_2III_2IV_2$ with the sub-region refinement density maps aligned. These maps are shown in three differently rotated views. View from the matrix side (upper), along the membrane (middle) and the 90 °flip around its vertical axis (lower). CI, $CIII_2$, CIV and *Cyt.c* are colored and labeled with texts in same colors, respectively.

b, Cartoon representation of two CIV movement among $MCI_2III_2IV_2$. Shown in two differently rotated views along the membrane. The dotted arrows indicate the shift of CIV in $MCI_2III_2IV_2$ of Mid 1-3. $CIII_2$, CIV and *Cyt.c* are colored and labeled with texts in same colors, respectively.

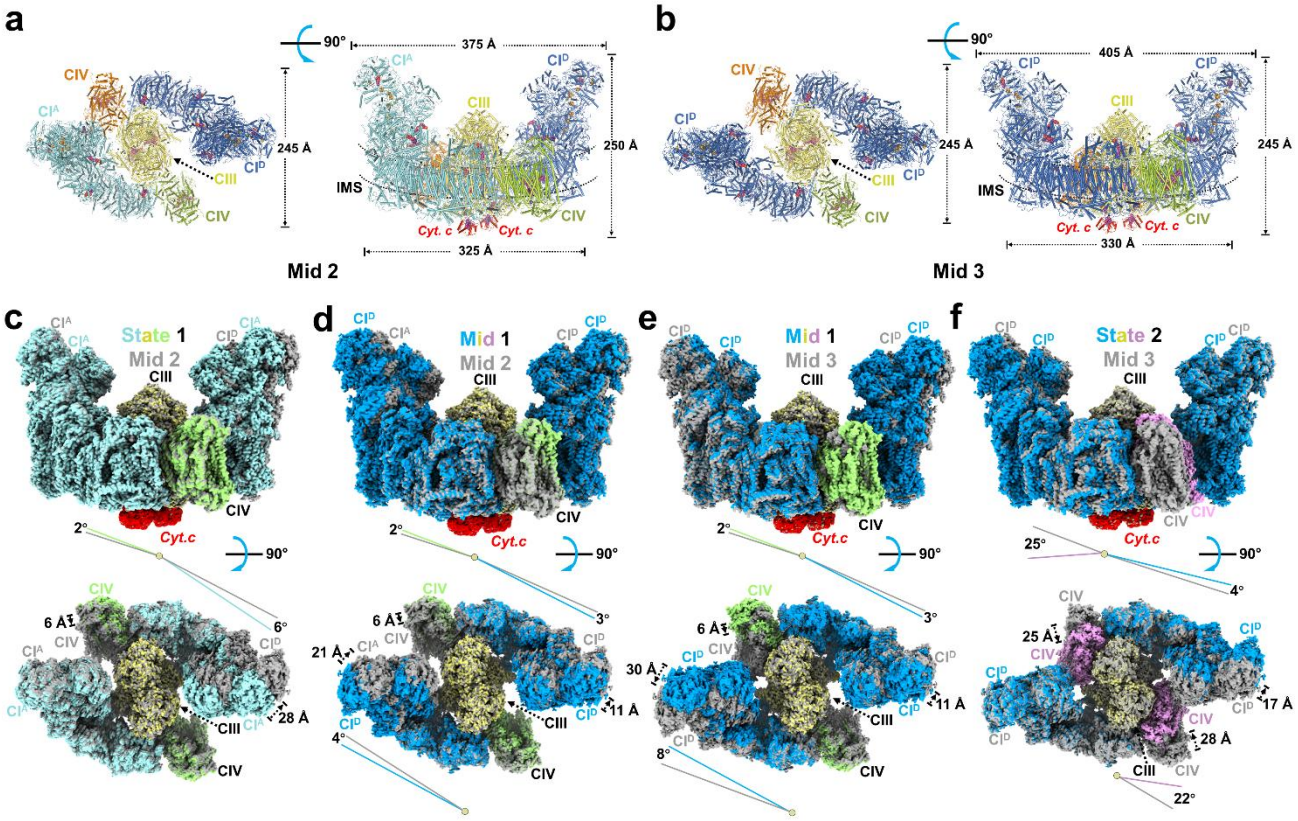

Extended Data Fig. 6 | Overall structures and comparison among $MCI_2III_2IV_2$ structures.

a-b, Cartoon representation of $MCI_2III_2IV_2$ structures of Mid 2 and Mid 3. The structure is shown in three differently rotated views (left, side view along the inner membrane; right, top view from the matrix side; bottom, bottom view from the intermembrane side). The transmembrane region is indicated by two dashed lines. IMS, intermembrane space. The cofactors are shown in spheres.

c-f, Comparison among porcine $MCI_2III_2IV_2$ maps of State 1, State 2, Mid 1-3. CI, $CIII_2$, CIV and *Cyt.c* are colored and labeled with texts in same colors, respectively. Shown in two differently rotated views along the intermembrane side.

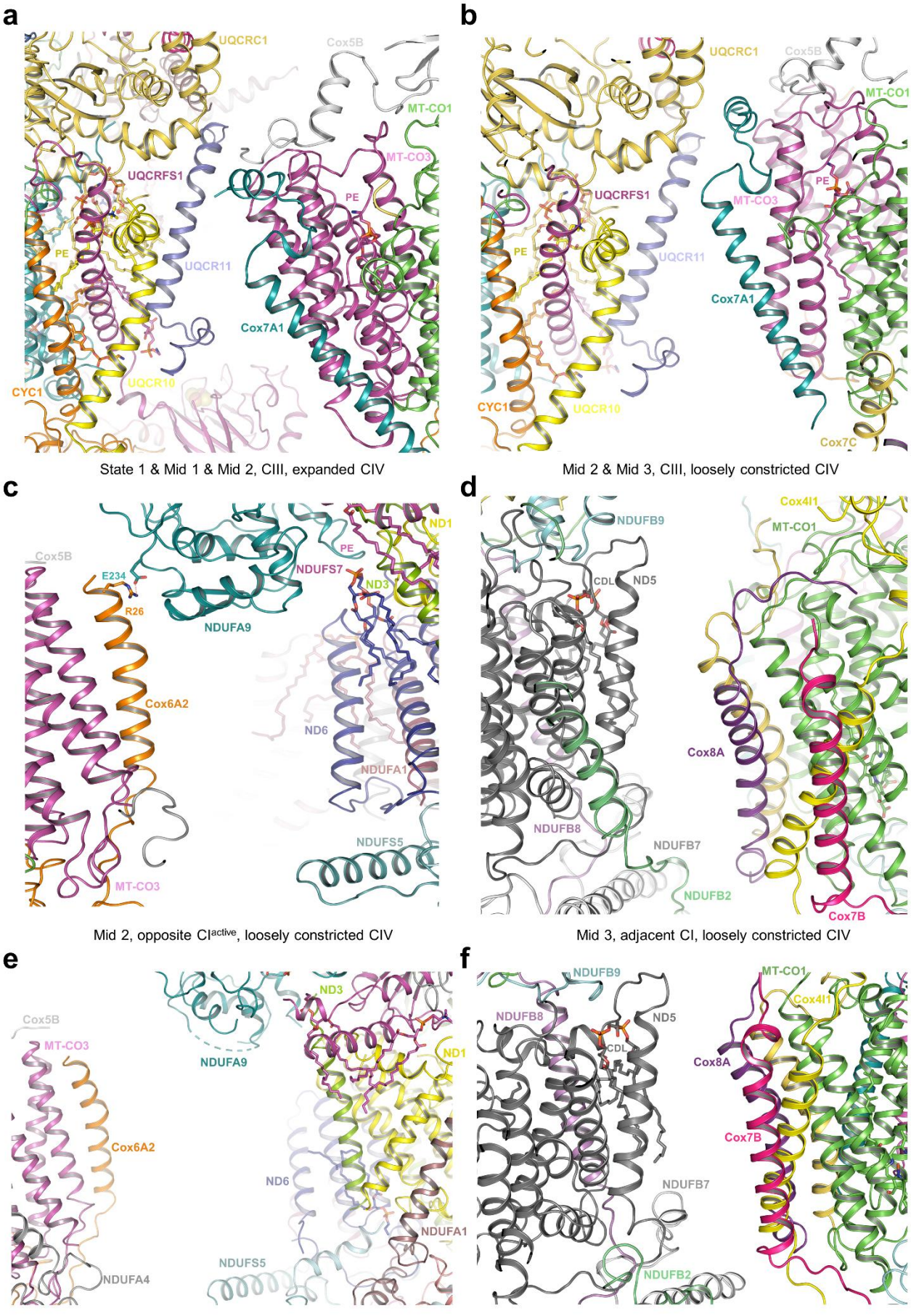
a
UQCRC1
Cox5B
MT-CO1
MT-CO3
UQCRFS1
PE
PE
UQCR11
Cox7A1
CYC1
UQCR10
State 1 & Mid 1 & Mid 2, CIII, expanded CIV
b
UQCRC1
Cox5B
MT-CO1
PE
UQCRFS1
MT-CO3
PE
UQCR11
Cox7A1
CYC1
UQCR10
Cox7C
Mid 2 & Mid 3, CIII, loosely constricted CIV
c
ND1
Cox5B
PE
E234
NDUFS7
ND3
R26
NDUFA9
Cox6A2
ND6
NDUFA1
NDUFS5
MT-CO3
Mid 2, opposite CI^active, loosely constricted CIV
d
NDUFB9
Cox4I1
MT-CO1
CDL
ND5
Cox8A
NDUFB8
NDUFB7
NDUFB2
Cox7B
Mid 3, adjacent CI, loosely constricted CIV
e
ND3
Cox5B
MT-CO3
NDUFA9
ND1
Cox6A2
ND6
NDUFA1
NDUFS5
NDUFA4
Mid 3, opposite CI, loosely constricted CIV
f
NDUFB9
MT-CO1
Cox4I1
NDUFB8
ND5
CDL
Cox8A
Cox7B
NDUFB7
NDUFB2
State 2, adjacent CI, constricted CIV

263

Extended Data Fig. 7 | Interactions between CIII-CIV and CI-CIV in $MCI_2III_2IV_2$.

a-b, The CIII-CIV interaction regions in $MCI_2III_2IV_2$ of State 1 and Mid 1-3. Subunits participating in the interactions are colored as labeled with texts in the same colors, respectively. The cofactors are shown in sticks.

a, The interactions between CIII and expanded CIV in State1 and Mid 1/2.

b, The interactions between CIII and loosely constricted CIV in Mid 2/3.

c-f, The CI-CIV interaction regions in $MCI_2III_2IV_2$. The subunits close to each other are colored as labeled with text in the same colors, respectively. The interaction residues are shown as sticks and indicated, respectively. The phospholipid molecules are shown in sticks.

c, The interactions between CI^{Active} and loosely constricted CIV in Mid 2. $NDUFA9^{E234}$ directly interacts with $Cox6A2^{R26}$ in the transmembrane region.

d, The interactions between adjacent CI and loosely constricted CIV in Mid 3.

e, The interactions between opposite CI and loosely constricted CIV in Mid 3.

f, The interactions between adjacent CI and constricted CIV in State 2.

Supplementary Table 1 | Cryo-EM data collection and model refinement									
	State 1	State 2	Mid 1	Mid 2	Mid 3	Active-CI	Deactive-CI	CIII	CIV
Data collection and processing									
EMDB code	XXXXX	XXXXX	XXXXX	XXXXX	XXXXX	XXXXX	XXXXX	XXXXX	XXXXX
PDB code	XXXX	XXXX	XXXX	XXXX	XXXX	XXXX	XXXX	XXXX	XXXX
Electron microscopy	Titan Krios								
Camera	Gatan K3 Summit								
Magnification	81,000								
Voltage	300 kV								
Defocus range (μm)	-1.7 to -2.5								
Electron exposure (e–/Å^2)	50								
Pixel size (Å)	1.1								
Exposure rate (e$^-$/A^2/sec)	20								
Number of frames per movie	40								
Energy filter slit width	20								
Automation software	SerialEM								
Micrographs collected	41,117								
Data processing software	RELION 3.1 & cryoSPARC 3.2						RELION 3.1		
Symmetry imposed	C2	C2	C2	C1	C1	C1	C1	C1	C1
Total extracted particles	2,733,141								
Total refined particles	10,060	28,288	35,332	22,749	18,992	32,827	74,952	99,312	32,007
Final particles	10,060	28,288	35,332	22,749	18,992	32,827	74,952	99,312	32,007
Map resolution (Å) at 0.143 FSC threshold	4.37	3.58	3.46	4.32	4.32	3.34	3.22	3.36	3.66
Local resolution range (Å)	3.5-7.5	3.0-5.5	3.0-5.5	3.5-6.5	3.5-6.5	2.4-4.5	2.4-4.5	3.0-5.5	3.0-5.5
Refinement									
Initial Model (PDB code)	5GUP/5XTI	5GUP/5XTI	5GUP/5XTI	5GUP/5XTI	5GUP/5XTI	7V2C	7V2D	5XTE	5Z62
Refinement Package	Phenix 1.19 (real space refinement)								
Model resolution (Å) at 0.5 FSC threshold	3.59	3.61	3.56	3.56	3.60	3.48	3.48	3.55	3.71
Map sharpening B factor (Å^2)	-20	-20	-20	-20	-20	-20	-20	-20	-20
Map CC	0.72	0.73	0.73	0.73	0.75	0.80	0.70	0.80	0.72
Model composition									
Non-hydrogen atoms	200,866	197,754	197,754	199,310	197,754	67,856	66,330	35,660	14,746
Protein residues	24,584	24,320	24,320	24,452	24,320	8,267	8,135	4,380	1,835
Ligands	109	95	95	103	97	35	29	31	6
B factors (Å^2)									
Protein	96.28	104.97	104.97	100.60	104.97	87.81	100.59	70.90	91.91
Ligands	85.21	91.34	91.34	87.92	91.34	87.99	99.71	99.69	81
R.m.s. deviations									
Bond lengths (Å)	0.009	0.009	0.009	0.009	0.009	0.008	0.008	0.007	0.003
Bond angles (°)	1.181	1.179	1.179	1.180	1.180	1.163	1.16	0.814	0.720
Validation									
MolProbity score	1.86	1.92	1.92	1.89	1.92	1.83	1.92	1.93	1.90
EMRinger score	1.53	1.61	1.65	1.69	1.60	1.74	1.85	1.92	1.74
Clashscore	10.40	11.23	11.02	10.69	11.11	9.08	9.94	7.88	10.95
Poor rotamers (%)	0	0	0	0	0	0	0	0	0
C-beta deviations	0	0	0	0	0	0	0	0	0
CaBLAM outliers	2.26	2.44	2.44	2.35	2.42	2.48	2.75	2.05	1.80
Ramachandran plot (%)									
Favored	95.39	94.83	94.83	95.12	94.95	94.95	94.09	95.55	96.40
Allowed	4.58	5.13	5.13	4.84	5.11	5.01	5.87	4.38	3.60
Outlier	0.04	0.04	0.04	0.04	0.04	0.04	0.04	0.07	0

280

Supplementary Table 2 | All the subunits of *Sus scrofa* complex III.

Subunit	Total residues	Chain	Mature protein	Modelled residues	Assigned residues	Sequence identity *H. sapiens/B. taurus/M. musculus*
UQCRC1	480	L/Y	35-480	35-480	35-480	88.75%,92.29%,87.71%
UQCRC2	453	K/W	15-453	35-453	35-453	88.30%,92.49%,84.99%
MT-CYB	379	J/V	1-379	1-379	1-379	76.68%,90.24%,85.53%
CYC1	326	H/U	86-326	86-326	86-326	95.46%,98.06%,94.82%
UQCRFS1N	78	O	1-78	1-75	1-75	87.18%,92.31%,85.90%
UQCRFS1	274	C/P	79-274	79-274	79-274	90.13%,95.26%,92.70%
UQCRB	111	F/S	2-111	6-111	6-111	87.39%,93.69%,88.29%
UQCRQ	82	A/N	2-82	2-82	2-82	82.93%,93.90%,84.15%
UQCRH	91	E/R	14-91	23-91	23-91	91.21%,95.60%,83.52%
UQCR10	64	D/Q	2-64	2-63	2-63	85.94%,95.31%,90.63%
UQCR11	56	G/T	1-56	2-54	2-54	83.93%,89.29%,94.64%
CYCS	105	B/Z	2-105	2-105	2-105	90.48%,100%,97.14%

281

Supplementary Table 3 | All the subunits of *Sus Scrofa* complex IV.

Subunit	Total residues	Chain	Mature protein	Modelled residues	Assigned residues	Sequence identity *H. sapiens/B. taurus/M. musculus*
MT-CO1	514	A	1-514	1-513	1-513	91.63%,96.50%,93.97%
MT-CO2	230	B	1-230	1-227	1-227	71.74%,94.78%,89.57%
MT-CO3	261	C	1-261	2-261	2-261	86.59%,93.10%,86.97%
Cox4I1	169	D	23-169	30-169	30-169	81.07%,95.86%,83.43%
Cox5A	152	E	44-152	48-152	48-152	88.16%,97.37%.88.82%
Cox5B	129	F	32-129	34-129	34-129	82.95%,92.25%,86.05%
Cox6A2	97	G	13-97	24-96	24-96	83.51%,92.78%,82.47%
Cox6B	86	H	2-86	5-86	5-86	86.05%,97.67%,94.19%
Cox6C	75	I	1-75	6-75	6-75	74.67%,86.67%,81.58%
Cox7A1	80	J	22-80	22-77	22-77	80.00%,93.75%,85.00%
Cox7B	80	K	25-80	30-78	30-78	80.00%,87.50%,81.25%
Cox7C	63	L	17-63	17-63	17-63	87.30%,96.83%,98.41%
Cox8A	69	M	26-69	26-68	26-68	66.67%,79.71%,81.16%
NDUFA4	82	N	1-82	3-81	3-46	52.44%,92.68%,91.46%

282

Supplementary Table 4 | The interactions between CI, CIII and CIV in $MCI_2III_2IV_2$.

	State 1	Mid 1	Mid 2	Mid 3	State 2
Hydrogen bond (< 4Å)					
CI-CIII	NDUFA11^{Y108}-UQCRQ^{R43} NDUFB9^{K55}-UQCRC1^{N55} NDUFB4^{R30}-UQCRC1^{E259}		NDUFB9$^{D56}{}_{active}$-UQCRC1^{R288} NDUFB9$^{D56}{}_{deactive}$-UQCRC1^{R288} NDUFB9$^{K55}{}_{deactive}$-UQCRC1^{D54} NDUFB9$^{T61}{}_{deactive}$-UQCRC1^{V262} NDUFB4$^{K28}{}_{active}$-UQCRC1^{K85} NDUFA11$^{Y108}{}_{deactive}$-UQCRQ^{R43}		
CI-CIV		ND5^{E503}-Cox7A1^{N50} ND5^{E503}-Cox7A1^{R54}	ND5$^{E503}{}_{active}$-Cox7A1^{R54} ND5$^{K512}{}_{active}$-Cox7A1^{G45} ND5$^{E503}{}_{deactive}$-Cox7A1^{R54} ND5$^{Y510}{}_{deactive}$-Cox7A1^{L39} NDUFB3$^{K35}{}_{active}$-Cox7A1^{D38} NDUFB3$^{K35}{}_{deactive}$-Cox7A1^{D36}		
CIII-CIV					UQCR11^{R15}-Cox7C^{S30} UQCR11^{W44}-Cox8A^{W57} MT-CYB^{I368}-Cox7A1^{I51}
Adjacent interactions (> 4Å, < 10Å)					
CI-CIII	NDUFB4^{E28}-UQCRC1^{K85} NDUFB4^{K85}-UQCRQ^{T32} NDUFA11^{H19}-UQCRQ^{Q65}	NDUFA11^{I16}-UQCRQ^{Y69} NDUFA11^{I17}-UQCRQ^{Y69} NDUFA11^{I17}-UQCRQ^{Y62} NDUFA11^{I19}-UQCRQ^{Y58} NDUFA11^{I76}-UQCRQ^{Y52} NDUFA11^{I79}-UQCRQ^{Y65}	NDUFB4$^{K31}{}_{active}$-UQCRC1^{E259} NDUFB4$^{E28}{}_{deactive}$-UQCRC1^{E259} NDUFB9$^{D56}{}_{active}$-UQCRC1^{R58} NDUFB9$^{Q62}{}_{active}$-UQCRC1^{F265} NDUFB9$^{K55}{}_{deactive}$-UQCRC1^{N55} NDUFA11$^{E17}{}_{deactive}$-UQCRQ^{W62} NDUFA11$^{E17}{}_{deactive}$-UQCRQ^{Q65} NDUFA11$^{R106}{}_{deactive}$-UQCRQ^{R43}	NDUFB4^{R30}-UQCRC1^{E259} NDUFB4^{S2}-UQCR10^{A2} NDUFB4^{K5}-UQCRFS1^{E105} NDUFB4^{K31}-UQCRC1^{E260} NDUFB4^{E28}-UQCRC1^{K85} NDUFA11^{Y108}-UQCRQ^{R43}	NDUFA11^{I76}-UQCRQ^{Y57}
CI-CIV	ND5^{E503}-Cox7A1^{N50} ND5$^{T480\text{-}Y515}$-Cox7A1 ND5^{K512}-Cox7A1^{N37}	ND5^{E503}-Cox7A1^{I51} ND5^{M499}-Cox7A1^{R54} ND5^{T507}-Cox7A1^{A47} ND5^{Y510}-Cox7A1^{N50}	ND5$^{E503}{}_{active}$-Cox7A1^{N50} ND5$^{E510}{}_{active}$-Cox7A1^{N50} ND5$^{E514}{}_{active}$-Cox7A1^{G45} ND5$^{E510}{}_{deactive}$-Cox7A1^{N50} ND5$^{E511}{}_{deactive}$-Cox7A1^{N37} NDUFB9$^{Y39}{}_{active}$-Cox7A1^{N37} NDUFB3$^{K35}{}_{active}$-Cox7A1^{D36} NDUFB3$^{R39}{}_{active}$-Cox7A1^{R36}	ND5^{E503}-Cox7C^{N33}	ND5^{Y510}-Cox7B^{K36}
CIII-CIV	UQCR11^{R15}-Cox6A2^{R29}	UQCRC1^{D437}-Cox5B^{G34} UQCRC1^{E443}-Cox7A1^{N24} UQCR11^{R15}-MT-CO3^{K157} UQCR11^{R15}-Cox6A2^{R29}	UQCR11^{R15}-Cox6A2^{R29} UQCR11^{R15}-MT-CO3^{K157} UQCR11^{R11}-Cox6A2^{R29} UQCR10^{R9}-Cox7A1^{E23} UQCRC1^{D437}-Cox5B^{G34}	UQCR11^{R15}-Cox7A1^{T48} UQCR11^{P8}-Cox7A1^{R25} UQCRC1^{E385}-Cox7A1^{K31}	UQCR11^{G7}-MT-CO1^{M1} UQCR11^{R11}-Cox7C^{S30} UQCRC1^{E443}-Cox8A^{R32} UQCRC1^{E385}-Cox7C^{K25} UQCRC1^{E435}-Cox8A^{R32} UQCRB^{R15}-Cox7A1^{N37} MT-CYB^{R15}-Cox7A1^{Y69}

283